Applied Catalysis B: Environmental 238 (2018) 161–167

Contents lists available at ScienceDirect

Applied Catalysis B: Environmental

journal homepage: www.elsevier.com/locate/apcatb

Amorphous $FeCoPO_x$ nanowires coupled to g-C_3N_4 nanosheets with enhanced interfacial electronic transfer for boosting photocatalytic hydrogen production

Peng Zhou[a,1], Jianping Lai[a,b,1], Yonghua Tang[a], Yuguang Chao[a], Fei Lin[a], Shaojun Guo[a,b,c,d,*]

[a] Department of Materials Science and Engineering, College of Engineering, Peking University, Beijing 100871, China
[b] The Beijing Innovation Center for Engineering Science and Advanced Technology, College of Engineering, Peking University, Beijing 100871, China
[c] Department of Energy and Resources Engineering, College of Engineering, Peking University, Beijing 100871, China
[d] Key Laboratory of Theory and Technology of Advanced Batteries Materials, College of Engineering, Peking University, Beijing 100871, China

ARTICLE INFO

Keywords:
Interface
Amorphous $FCoPO_x$
Nanowire
g-C_3N_4
Electron transfer

ABSTRACT

The building of an optimized interface between the cocatalyst and the photoactive materials is significant for understanding the charge transfer mechanism and designing high-performance catalysts at atomic level, however, still a great challenge. Herein, we develop a new method to synthesize a class of hybrid photocatalyst by coupling amorphous $FeCoPO_x$nanowires ($FeCoPO_x$(NWs)) to$g$-C_3N_4 photocataysts (denote as $FeCoPO_x$(NWs)-C_3N_4) for greatly boosting the photocatalytic activity, which shows 3.5-fold higher H_2-production activity than the state-of-art crystalline $FeCoPO_y$ nanoparticles/g-C_3N_4 hybrid photocataysts (denote as $FeCoPO_y$(NPs)-C_3N_4). The structure analysis by X-ray absorption fine structure (XAFS) reveals that the Fe species in $FeCoPO_x$(NWs)-C_3N_4 owns a lower coordination number than that in $FeCoPO_y$(NPs)-C_3N_4, which can contribute to the formation of strong interface between $FeCoPO_x$(NWs) and g-C_3N_4. The first-principles simulation confirms that the amorphous $FeCoPO_x$(NWs) not only can build a stable interface with g-C_3N_4 by forming more Fe-N bonds, but also own an optimized electronic properties for enhancing electron transfer from g-C_3N_4 to $FeCoPO_x$(NWs). The strong interfacial electronic effect of $FeCoPO_x$(NWs)-C_3N_4 contributes to its high H_2-production activity.This work not only develops a new method to prepare the high-performance low-cost cocatalyst as Pt alternative for H_2 production, but also provide a new insight into optimizing the interface between cocatalyst and photocatalyst for photocatalytic reaction.

1. Introduction

Photocatalytic water splitting represents a promising strategy for clean, low-cost and environmental friendly production of hydrogen (H_2) by utilizing solar energy. There are three crucial steps for the photocatalytic water splitting reaction: solar light harvesting, charge separation and transportation, and the intrinsic catalytic H_2 and O_2 evolution reactions [1,2]. To date, significant achievements have been made in making the efficient visible-light-response photocatalysts and optimizing the O_2/H_2-evolution performance of cocatalyst in the photocatalytic process [3,4]. However, much less efforts have been devoted to improving the efficiency of the second step, which demands an optimized interface between cocatalyst and photocatalyst [5–7]. Especially, the reported H_2-evolution cocatalysts usually employ expensive noble metal (such as Pt and Pd) [8,9].

In recent years, the cheap and earth-abundant cocatalysts with low overpotential, in particular the phosphide of VII elements, for H_2 evolution have been demonstrated to exhibit good hydrogen evolution activity [10,11]. However, the performance of photocatalyst using earth-abundant cocatalysts is still quite low relative the benckmark noble metal catalyst due to the two main reasons: one is that the phosphide of VII elements with low work function, unlike noble metal, easily suffers from a difficulty in capturing the photogenerated electrons from photocatalyst, and the other is that the phosphide easily suffers from the light corrosion, easily leading to the deactivation of cocatalyst. In this regards, developing a cocatalyst with strong electron-capturing ability and high stability is highly required for the practical photocatalytic application. It is well known that the charge transfer

* Corresponding author at: Key Laboratory of Theory and Technology of Advanced Batteries Materials, College of Engineering, Peking University, Beijing 100871, China.

E-mail address: guosj@pku.edu.cn (G. Shaojun).

[1] Peng Zhou and Jianping Lai contributed equally.

https://doi.org/10.1016/j.apcatb.2018.07.007
Received 23 March 2018; Received in revised form 21 June 2018; Accepted 2 July 2018
Available online 03 July 2018
0926-3373/

between cocatalyst and photocatalyst strongly depends on the electronic properties of interface between them [12,13]. Thus, an optimized interface between cocatalyst and photocatalyst is definitely highly desirable forboosting the electron transfer channel in the photocatalytic path to achieve much better photocatalytic performance for hydrogen production.

Herein, we used an amorphous $FeCoPO_x$ nanowires ($FeCoPO_x$(NWs)) to replace the common crystalline $FeCoPO_y$ nanoparticles ($FeCoPO_y$(NPs)) as the H_2-production cocatalyst to greatly boost the photocatalytic hydrogen evolution performance of g-C_3N_4. The results found that the coupled $FeCoPO_x$(NWs)/g-C_3N_4 ($FeCoPO_x$(NWs)-C_3N_4) owns a 3.5-fold higher H_2-production activity than the crystalline $FeCoPO_y$ nanoparticles/g-C_3N_4 hybrid photocataysts (denote as $FeCoPO_y$(NPs)-C_3N_4) in the photocatalytic hydrogen production, similar to that of expensive Pt-loaded g-C_3N_4 (Pt-C_3N_4). The X-ray absorption fine structure (XAFS) measurements confirm that the Fe species in $FeCoPO_x$(NWs)-C_3N_4 owns a lower coordination number than that in $FeCoPO_y$(NPs)-C_3N_4, which is beneficial to the formation of stable interface between $FeCoPO_x$(NWs) and g-C_3N_4 after annealing the hybrids. Consistent with the experimental observation, the first-principles simulation reveals that the amorphous $FeCoPO_x$(NWs) is anchored on g-C_3N_4 by forming more Fe-N bonds due to the metastable feature of amorphous $FeCoPO_x$(NWs) than that of crystalline $FeCoPO_y$(NPs). As a result, an enhanced coupling interface tends to be formed between the amorphous $FeCoPO_x$(NWs) and g-C_3N_4. Besides, the Fe 3d states in amorphous $FeCoPO_x$(NWs) own a higher polarization than those in the crystalline $FeCoPO_y$, also contributing to the enhanced electron transfer from g-C_3N_4 to $FeCoPO_x$(NWs) for promoting the photocatalysis.

2. Experimentaland theoretical section

2.1. Chemicals

All of the reagents were of analytical grade and were used without further purification. $Fe(CO)_5$, $Co_2(CO)_8$, phenylphosphine (TOP), oleylamine and 1-octadecene were supplied by Sigma-Aldrich (Shanghai, China). Dicyandiamide, $Co(NO_2)_2$, $Fe(NO_3)_3$ and NaH_2PO_3 were purchased from Aladdin (Shanghai, China). Deionized (DI) water was used in all experiments.

2.2. Materials synthesis

Synthesis of g-C_3N_4. g-C_3N_4 photocatalysts was prepared following a typical thermal polymerization procedure [14]. Briefly, 5 g of dicyandiamide was put into a covered crucible, heated to500 °C at a ramp rate of 5 °C min^{-1} in a muffle furnace and then maintained at this temperature for additional 2 h. After being cooled down to room temperature, the resultant powders was ultrasonicated with deionized water, collected by filtration and finally dried under vacuum at 60 °C.

Synthesis of ultrathin $FeCoPO_x$(NWs). $Fe(CO)_5$ (0.1 mL) and $Co_2(CO)_8$ (10 mg) were dissolved in 5 mL of TOP at 60 °C for 1 h. At the same time, 10 mL of oleylamine and 2 mL of 1-octadecene were placed in a 50 mL Schlenk flask with a condenser. The system was degassed at 120 °C for 20 min to remove any moisture or oxygen, followed by purging with N_2 for 30 min. The mixture in TOP was injected into the system. The system was further heated to300 °C (under N_2) at a rate of approximately 8 °C min^{-1} and maintained at 300 °C for 1 h. The black precipitate was sonicated in hexane and reprecipitated with isopropanol. This sonication − precipitation cycle was performed at least two times to remove as much of the bound organics as possible from the system. Finally, the isolated black powder was dispersed in 20 mL hexane for further application.

Synthesis of $FeCoPO_x$(NWs)-C_3N_4. 3 mL of FeCoP(NWs) hexane solution and 0.2 g of g-C_3N_4 was mixed in 100 mL of ethanol under magnetic stirring for 30 min. Next, the mixed solution was ultrasonicated for 30 min, and then transferred into oil bath at 70 °C. After drying, the left solid was collected. To build a stable interface between g-C_3N_4 and $FeCoPO_x$(NWs), the obtained samples placed in crucible and then heated to 400 °C at a ramp rate of 5 °C min^{-1} in a muffle furnace under N_2 atmosphere. After being cooled down to room temperature, the resultant powders was collected for following tests.

Synthesis of $FeCoPO_y$(NPs)-C_3N_4. In a typical synthesis, an aqueous suspension of g-C_3N_4 was first prepared by dispersing 0.2 g g-C_3N_4 into 100 mL deionized water with sonication, and then transferred into oil bath at 70 °C. Then, 0.9 mL of $Fe(NO_3)_3$ aqueous solution (0.1 mol L^{-1}) and 0.05 mL of $Co(NO_3)_2$ aqueous solution (0.1 mol L^{-1}) was added into the g-C_3N_4 aqueous dispersion, and keptstirring for 18 h to dry. Finally, the dried solid was collected. The obtained impregnated sample was placed in the tube furnace, and annealed at 400 °C for 2 h in N_2 atmosphere. The $FeCoPO_y$(NPs)-C_3N_4 sample was synthesized using sodium hypophosphite($NaH_2PO_2{\cdot}H_2O$) as the P precursor. Specifically, 0.1 g of the as-prepared sample and 0.1 g of sodium hypophosphite were mixed together and finely grind with a motar. Then, the mixture was heated at 300 °C for 2 h in N_2 atmosphere at a ramp rate of 5 °C/min. Generally, $NaH_2PO_2{\cdot}H_2O$ will decompose togenerate PH_3 at temperature higher than 200 °C, which can phosphorize the oxides of Fe and Co on g-C_3N_4. Finally, the obtained sample was collected.

2.3. Catalyst characterization

The X-ray diffraction (XRD) patterns, obtained on an X-ray diffractometer (Rigaku, Japan) using Cu Kα radiation at a scan rate of 0.05° 2θ s^{-1}, were used to characterize the crystalline phase of the samples. The accelerating voltage and applied current were 40 kV and 80 mA, respectively. High-resolution scanning transmission electron microscopy (HRSTEM) analysis was conducted on JEOL 2100 F transmission electron microscope with a 300 kV accelerating voltage. X-ray photoelectron spectroscopy (XPS) measurements were performed on an ESCALAB 250Xi electron spectrometer with Mg Kα (1253.6 eV) source. All binding energies were referenced to the C 1 s peaks at 284.8 eV from the adventitious carbon. Electron spin resonance (ESR) experiments were conducted on an ER-200D spectrometer (Bruker, Germany) at a microwave frequency of 9.5 GHz under room temperature. The content of Fe, Co, P and Pt elements in the as-prepared sampleswere analyzed by an inductively coupled plasma-atomic emission spectrometer (ICP-AES) on PerkinElmer Optima 7300DV.

2.4. XAFS measurement and data analysis

XAFS spectra at the Fe K-edge (7709 eV) were measured at the 1W1B beamline of Beijing Synchrotron Radiation Facility (BSRF), China. The storage ring of BSRF was working at the energy of 2.5 GeV with a maximum electron current of 250 mA. The hard X-ray was monochromatized with Si(111) double-crystal monochromator and the detuning was done by 30% to remove harmonics. The acquired EXAFS data were processed according to the standard procedures using the ATHENA module implemented in the IFEFFIT software packages. The k^3-weighted $\chi(k)$ data in the k-space ranging from 2.0 to 10.65 $Å^{-1}$ were Fourier transformed to real (R) space using a hanning windows ($dk = 1.0$ $Å^{-1}$) to separate the EXAFS contributions from different coordination shells. To obtain the detailed structural parameters around Fe atom in the as-prepared samples, quantitative curve-fittings were carried out for the Fourier transformed $k^3\chi(k)$ in the R-space using the ARTEMIS module of IFEFFIT3. Effective backscattering amplitudes F(k) and phase shifts $\Phi(k)$ of all fitting paths were calculated by the ab initio code FEFF8.0. During the fitting analysis, the amplitude reduction factor S_0^2 was fixed to the best-fit value of 0.70, which was determined from fitting the reference sample of Fe_2O_3 bulk and FeP bulk. To fit the data of $FeCoPO_y$(NPs)-C_3N_4 and $FeCoPO_x$(NWs)-C_3N_4 samples, the interatomic distance (R) and the Debye-Waller factor (σ^2) were allowed to vary. We have distinguished Fe-O from Fe-P coordination, considering

the existing bonding length difference between them. Thus two separate paths were used, which were corresponding to Fe-P pair in FeP and Fe-O in Fe_2O_3, respectively.

2.5. Catalytic activity measurements

The photocatalytic H_2-production experiments were performed in a doublelayered Pyrex vessel (inner volume 50 mL with diameter of 36 mm and height of 50 mm). A 300 W Xe lamp with the light filter of 420 nm and IR was used as the light source. The focused intensity on the flask was ~ 100 mW·cm^{-2}, which was measured by a FZ-A visible-light radiometer (made in the photoelectric instrument factory of Beijing Normal University, China) with a wavelength range of 400-1000 nm. In a typical photocatalytic H_2-production experiment, 20 mg of the prepared photocatalyst was suspended in 100 mL 10 vol% triethanolamine aqueous solution, and then bubbled with Ar through the reactor for 30 min to completely remove the dissolved oxygen and ensure the reactor was in an an aerobic condition. A continuous magnetic stirrer was applied at the bottom of the reactor to keep the photocatalyst particles in suspension during the experiments. A thermostatic digital controller (HX-205) was employed to control the reaction temperature. The amount of produced H_2 is tested every hour. 1 mL of gas sample was sampled from the headspace of the flask through the septum. H_2 content was analyzed by gas chromatography (GC-7890B, Agilent, America, TCD, with Ar as acarrier gas and 5 Å molecular sieve column), which was used to evaluate the H_2-production activity of different samples. All glassware was carefully rinsed with DI water prior to use.

2.6. Photoelectrochemical measurements

Photocurrent was measured on an CHI650D instrument in the three-electrode system using the as-prepared samples as the working electrodes, Ag/AgCl as the reference electrode, and the Pt wire as the-counter electrode. 0.5 M Na_2SO_4 aqueous solution was utilized as the electrolyte. A 300 W Xe light with a light filter of 420 nm was applied as the light source. The working electrodes were synthesized as follows: 10 mg sample was dispersed in8 mL of 75 vol% isopropanol aqueous solution containing 50 μLof Nifon to make a slurry. Then 100 μLof slurry was coated onto a 1 cm × 3 cm FTO glass electrode. The obtained electrode was dried in an oven at 333 K for 0.5 h. Electrochemical Impedance Spectroscopy (EIS) measurements were recorded over a range from 0.001 to 2×10^5 Hz with an AC amplitude of 0.02 V.

2.7. Theoretical simulation

The photocatalytic charge transfer mechanism between $FeCoPO_y$(NPs)/$FeCoPO_x$(NWs) and g-C_3N_4 was investigated by the density functional theory (DFT) calculations based on the VASP package using the PBE exchange-correlation function [15,16].The interaction between valence electrons and the ionic core was described by the PAW pseudo-potential. The model of $FeCoPO_y$(NPs) with low O content was only simulated by a crystalline FeCoP nanoparticle containing 54 Fe atoms, 2 Co atoms and 56 P atoms, obtained from the structure of orthorhombic FeP bulk. However, considering the existence of numerous O atoms in the experiments, the models of $FeCoPO_x$(NWs) was simplified by an amorphous nanoparticle containing 56 Fe atoms, 2 Co atoms, 47 P atoms and 9 O atoms. As for the model of g-C_3N_4, a periodic atomic layer containing 96 C atoms and 128 N atoms was built. Before the projected density of states (PDOS) calculations, the models were optimized with the cutoff of 400 eV. All the atoms in the model were allowed to adjust until the magnitude of all residual forces was less than 0.001 eV/Å. Considering the calculation cost, the geometry optimization was only performed at Gamma point. After the geometry optimization, the PDOS was calculated by the cutoff energy of 400 eV and the Monkhorst-Pack k-point mesh of 2 × 2 × 1 [17]. Besides, the iso-surfaces of interface between $FeCoPO_y$(NPs)/$FeCoPO_x$(NWs) and g-C_3N_4 were constructed by calculating the charge density differences of the $FeCoPO_y$(NPs)/$FeCoPO_x$(NWs) model (ρ_{FeCoP} (r)), the g-C_3N_4 model (ρ_{C3N4} (r)) and the whole model ($\rho_{FeCoP+C3N4}$(r)):

$$\rho_{difference}(r) = \rho_{FeCoP+C3N4}(r) - \rho_{FeCoP}(r) - \rho_{C3N4}(r)$$

The obtained charge density differences were used to describe the bonding properties of the interface between $FeCoPO_y$(NPs)/$FeCoPO_x$(NWs) and g-C_3N_4.

3. Results and discussion

The $FeCoPO_x$ nanowires were first synthesized in the oleylamine solution with $Fe(CO)_5$/$Co_2(CO)_8$ as Fe/Co source and triphenylphosphine (TOP) as P source. Transmission electron microscopy (TEM) images show that the $FeCoPO_x$ nanowires have an average diameter of 4 nm (Fig. S1). It should be noted that the slightCo is mainly used to adjust the morphology of $FeCoPO_x$ nanowires. Then, a certain amount of amorphous $FeCoPO_x$ nanowires cyclohexane solution were mixed with g-C_3N_4 ethanol suspension (Fig. S2) to obtain $FeCoPO_x$(NWs)/C_3N_4 hybrids by sonication, followed by being calcined at 400 °C in N_2 atmosphere. In the calcining process, the N/C atoms in g-C_3N_4 can be coordinated to the unsaturated Fe atoms in amorphous $FeCoPO_x$ (NWs). Especially, the low-coordinated N with stronger binding ability can promote the formation of more Fe-N bonds in the interface between $FeCoPO_y$(NWs) and g-C_3N_4. The TEM image shows that the $FeCoPO_x$ nanowires are well supported on g-C_3N_4 (Fig. 1a). The high-resolution TEM (HRTEM) image shows that no clear lattice fringe is observed in $FeCoPO_x$(NWs) (Fig. 1b). The corresponding selected area electron diffraction (SAED) image confirms its amorphous feature (*inset* in Fig. 1b). The scanning transmission electron microscopy (STEM) and the corresponding energy dispersive spectroscopy (EDS) mapping shows that Fe, Co and P elements are homogeneously distributed in the $FeCoPO_x$ nanowires. Besides, the remarkable O element also appears in the region of FeCoP nanowires due to the metastability of amorphous structure [18,19].

For acomparison, the crystalline $FeCoPO_y$ nanoparticles ($FeCoPO_y$(NPs)) was synthesized by a common phosphorization method [14,20]. In a typical process, the $Fe(NO_3)_2$ and $Co(NO_3)_2$ as the metal precursors were firstly impregnated into g-C_3N_4, followed by the calcination at 400 °C to form the oxides of Fe and Co, noted as FeCoO (NPs). The obtained FeCoO-loaded g-C_3N_4 was mixed with NaH_2PO_2 and further calcined at 300 °C. The PH_3, released from the pyrolysis of NaH_2PO_2, directly reduced FeCoO into $FeCoPO_y$. The TEM images show that the $FeCoPO_y$(NPs) are well dispersed on g-C_3N_4 (Fig. S3a). The corresponding HRTEM image shows the lattice spacing (2.4 Å) of the crystals (Fig. S3b), indicating the existence of nanocrystalline phases. The SAED pattern (*inset* of Fig. S3b) reveal an orthorhombic structure (space group Pna21), consistent with the structure of FeP.

It should be noted that $FeCoPO_y$(NPs)-C_3N_4 and $FeCoPO_x$(NWs)-C_3N_4 own similar Fe, Co and P contents by controlling the added $FeCoPO_x$(NWs), $Fe(NO_3)_2$, $Co(NO_3)_2$ and NaH_2PO_2 contents according to the ICP measurement (Table S1). The content of Co in $FeCoPO_x$(NWs)-C_3N_4 is slightly lower than that in $FeCoPO_y$(NPs)-C_3N_4. However, compared to the Fe content, the Co content is negligible. X-ray diffraction (XRD) patterns of the bare g-C_3N_4, $FeCoPO_y$(NPs)-C_3N_4 and $FeCoPO_x$(NWs)-C_3N_4 all show a diffraction peak at 27.2° (Fig. S4), indexed to the typical g-C_3N_4 as reported previously [21,22]. However, the diffraction peak of $FeCoPO_x$ or $FeCoPO_y$ does not appear due to its low content. The UV-vis diffuse reflectance spectra (DRS) for the bare g-C_3N_4, $FeCoPO_y$(NPs)-C_3N_4 and $FeCoPO_x$(NWs)-C_3N_4 reveal that a progressive redshift in the absorption edge is achieved after $FeCoPO_x$ or $FeCoPO_y$ loading (Fig. S5a). The bandgaps of the samples determined from the transformed Kubelka-Munk function progressively narrow from 2.56 eV to 2.31 eV for $FeCoPO_y$(NPs)-C_3N_4 and 2.14 eV for $FeCoPO_x$(NWs)-C_3N_4 (Fig. S5b). This redshift results from the light adsorption of $FeCoPO_x$ or $FeCoPO_y$ instead of g-C_3N_4 since FeCoP is black

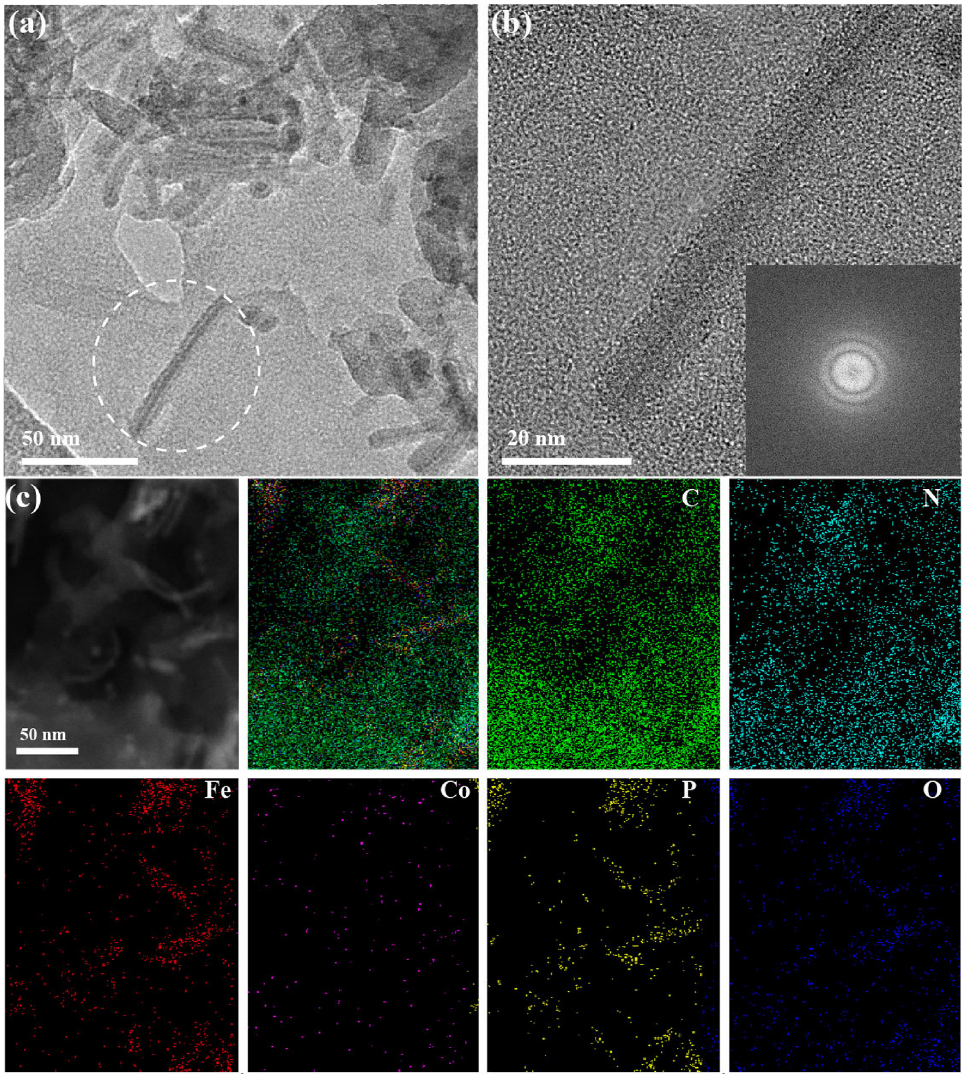

Fig. 1. Morphology and structure characterization of $FeCoPO_x$(NWs)-C_3N_4: (a) TEM, (b) HRTEM and (c) STEM images and corresponding EDX mapping.

and can easily absorb visible light. N_2 physisorption measurements were used to examine the specific surface area and pore structure of different samples. The isotherms of the $FeCoPO_y$(NPs)-C_3N_4 and Fe-$CoPO_x$(NWs)-C_3N_4 both have the obvious hysteresis loops at high relative pressure between 0.8 and 1.0, defined as type II mesoporous solids according to the Brunauer-Deming-Deming-Teller (BDDT) classification (Fig. S5c). The BET specific surface areas (BET) determined for $FeCoPO_y$(NPs)-C_3N_4 and $FeCoPO_x$(NWs)-C_3N_4 were 35 and 38 $m^2\,g^{-1}$, respectively. Besides, the pore sizes of as-prepared samples share the same distribution around 40 nm (Fig. S5d).

The X-ray photoelectron spectroscopy (XPS) was used to analyse the chemical state of surface atoms in $FeCoPO_y$(NPs)-$C_3N_4$and $FeCoPO_x$(NWs)-C_3N_4 samples. The main peaks at the 724.3 and 710.7 eV in the two samples correspond to the Fe $2p_{1/2}$ and $2p_{3/2}$ states of phosphatized Fe species, respectively (Fig. 2a) [23,24]. However, the peaks at the 729.3 and 714.6 eV are attributed to the Fe $2p_{1/2}$ and $2p_{3/2}$ states in oxidized Fe species. It is not strange that the surface of FeP is easy to be oxidized, especially in the $FeCoPO_x$(NWs)-C_3N_4 [24]. Besides, the weak Co 2p peaks at 789.3 and 783.7 eV are also observed (Fig. S6a), corresponding to the oxidized and phosphatized Co species, respectively. The high-resolution spectrum of P 2p shows a main peak at 133.3 eV, which is attributed to the P species in the type of Fe-P-O (Fig. 2b). However, a weak peak at 129.5 eV is caused by a typical P species in the type of Fe-P-Fe. The high-resolution spectrum of O 1 s reveals that two peaks at 532.7 eV and 531.1 eV are observed in the $FeCoPO_y$(NPs)-$C_3N_4$and $FeCoPO_x$(NWs)-C_3N_4 samples (Fig. 2c). Especially, the peaks at 531.1 eV in $FeCoPO_x$(NWs)-C_3N_4 is stronger than that in $FeCoPO_y$(NPs)-C_3N_4, which is corresponding to the O species in the Fe-O coordination. However, the peak at 532.7 eV can be attributed to the O species in the P-O coordination. The high-resolution spectra of C 1 s at 288.3 eV and N 1 s at 398.7 eV correspond to the C atoms in NC=N coordination and the two-coordinated N atoms in the framework of g-C_3N_4 (Fig. S6b and S6c), respectively [25]. Moreover, the electron spin resonance (ESR) was used to analyse the coordination of metal center. The results found that a stronger g factor at 2.003 is observed in $FeCoPO_x$(NWs)-C_3N_4 (Fig. 2d), indicating the existence of numerous defects [26]. This is consistent with the amorphous feature of $FeCoPO_x$(NWs)-C_3N_4.

X-ray absorption fine structure (XAFS) measurements were carried out to further investigate the structure of Fe species in atomic level. Fig. 2e shows Fe K-edge X-ray absorption near-edge structure (XANES) spectra of $FeCoPO_y$(NPs)-C_3N_4 and $FeCoPO_x$(NWs)-C_3N_4. The absorption edge of $FeCoPO_x$(NWs)-C_3N_4 is higher than that of $FeCoPO_y$(NPs)-C_3N_4. The Fourier-transformed (FT) k^3-weighted extended X-ray absorption fine structure (EXAFS) spectra reveal that one main peak at 1.5 Å corresponds to the first coordination shell (Fig. 2e). To obtain the quantitative chemical configuration of Fe atom, EXAFS fitting was also performed to extract the structure parameters (Fig. S7a and S7b). For

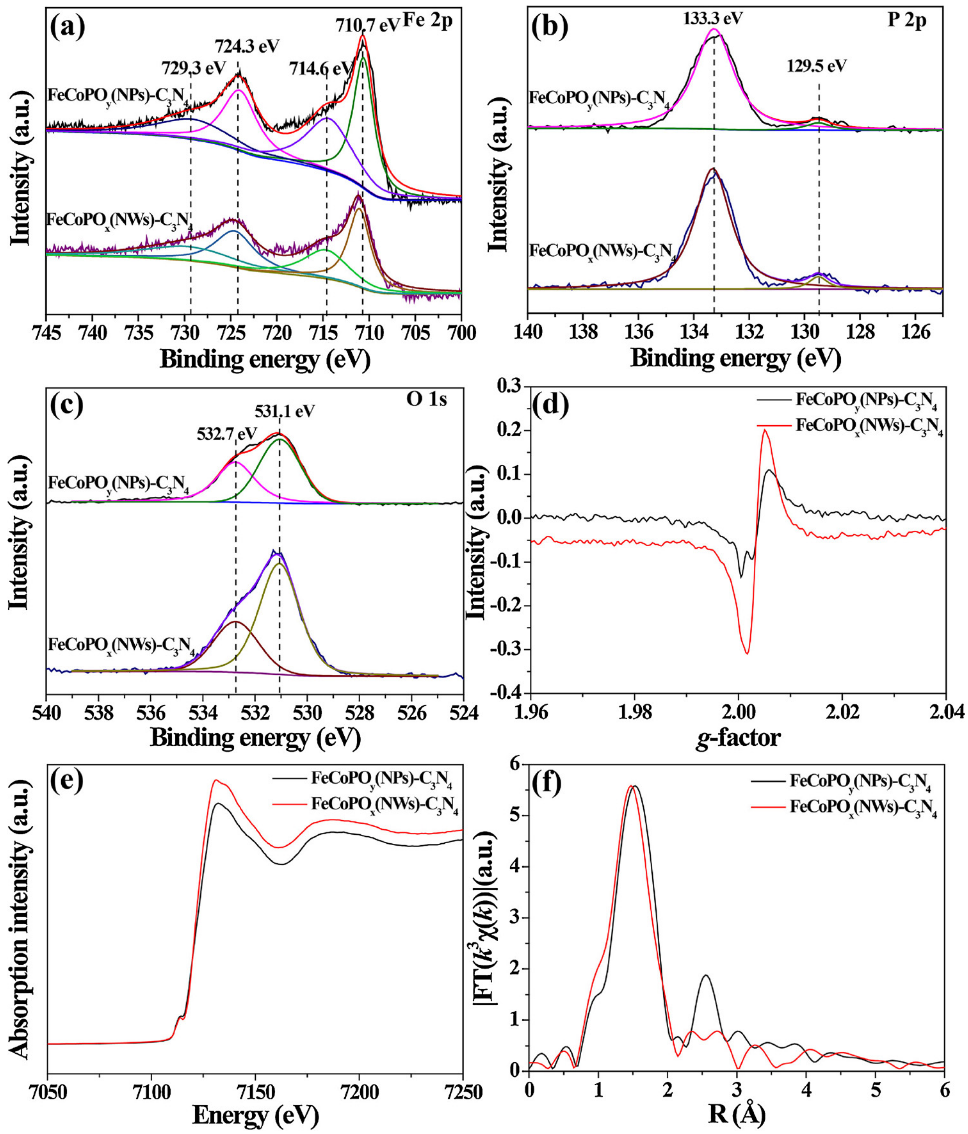

Fig. 2. Structure characterization of $FeCoPO_y$(NPs)-C_3N_4 and $FeCoPO_x$(NWs)-C_3N_4. XPS survey spectra of (a) Fe 2p, (b) P 2p and (c) O 1 s. (d) ESR signals at room temperatures. (e) Fe K-edge XANES spectra and (f) the corresponding k^3-weighted FT spectra.

$FeCoPO_y$(NPs)-C_3N_4 sample, the center Fe atoms own three coordinating interactions: Fe-P and Fe-O (Table S2). The coordination number is 4.85 for Fe-P and 1.58 for Fe-O. The mean bond lengths of Fe-P and Fe-O are 2.26 and 2.00 Å, respectively. However, for $FeCoPO_x$(NWs)-C_3N_4 sample, the coordination numbers of center Fe atoms are 0.54 for Fe-P and 3.48 for Fe-O. The mean bond lengths of Fe-P and Fe-O are 2.33 and 1.96 Å, respectively. This suggests that Fe-O bonds have a higher content in $FeCoPO_x$(NWs)-C_3N_4 than $FeCoPO_y$(NPs)-C_3N_4. Thus *x* is larger than *y*, which is also consistent with the STEM and XPS results. Especially, the total coordination number of Fe species in $FeCoPO_x$(NWs)-C_3N_4 is obvious lower than that in $FeCoPO_x$(NWs)-C_3N_4. Besides, the wavelet transform (WT) is used to analyse Fe K-edge EXAFS oscillations (Fig. S8). The WT maximum at 5.24 $Å^{-1}$ for $FeCoPO_y$(NPs)-C_3N_4 and 5.41 $Å^{-1}$ for $FeCoPO_x$(NWs)-C_3N_4 could be assigned to the Fe-P bonding, which also confirm the different coordination environment of Fe species in the two samples. Consequently, combining HRTEM, ESR and XAFS results, we can conclude that the coordination structure of Fe species in $FeCoPO_x$(NWs)-C_3N_4 are different from those in $FeCoPO_y$(NPs)-C_3N_4.

The photocatalytic H_2-production activities of the samples were measured in a double layered Pyrex vessel under irradiation of a 300 W Xe lamp with a 420 nm cutoff filter and by using triethanolamine as the electron donor. The results reveal that the oxidized Fe and Co species only shows little H_2 production (Fig. 3a). Further phosphorization treatment remarkably promotes H_2 production over $FeCoPO_y$(NPs)-C_3N_4, which exhibits a H_2-production activity of 180 μmol g^{-1} h^{-1}. However, the $FeCoPO_x$(NWs)-C_3N_4 sample shows 3.5 times higher H_2-production rate (687 μmol g^{-1} h^{-1}) than $FeCoPO_y$(NPs)-C_3N_4. Besides, the $FeCoPO_x$(NWs)-C_3N_4 sample owns a similar H_2-production activity with the Pt(1.48 wt%)-loaded C_3N_4 (Pt-C_3N_4) sample (Fig. 3a). The H_2-production stability test confirms that the $FeCoPO_x$(NWs)-C_3N_4 sample can stably work for 16 h with no obvious activity decrease (Fig. 3b). This suggests that the coupled $FeCoPO_x$(NWs)-C_3N_4 sampleis an idea cocatalyst for H_2 production, which can replace noble Pt catalyst. The photocurrent response and EIS measurements are performed to investigate the reason for the enhanced H_2-production activity of $FeCoPO_x$(NWs)-C_3N_4 compared to the $FeCoPO_y$(NPs)-C_3N_4. The transient photocurrent responses are conducted with interval 60 s light on/off cycle at 0 V *vs.* Ag/AgCl (Fig. 3c). The $FeCoPO_x$(NWs)-C_3N_4 shows an excellent photo-stability in the test and achieves a higher cathodic photocurrent than the bare *g*-C_3N_4 or $FeCoPO_y$(NPs)-C_3N_4, indicating that the addition of $FeCoPO_x$(NWs) promotes the electron transfer and separation process. EIS measurements provide additional evidence for

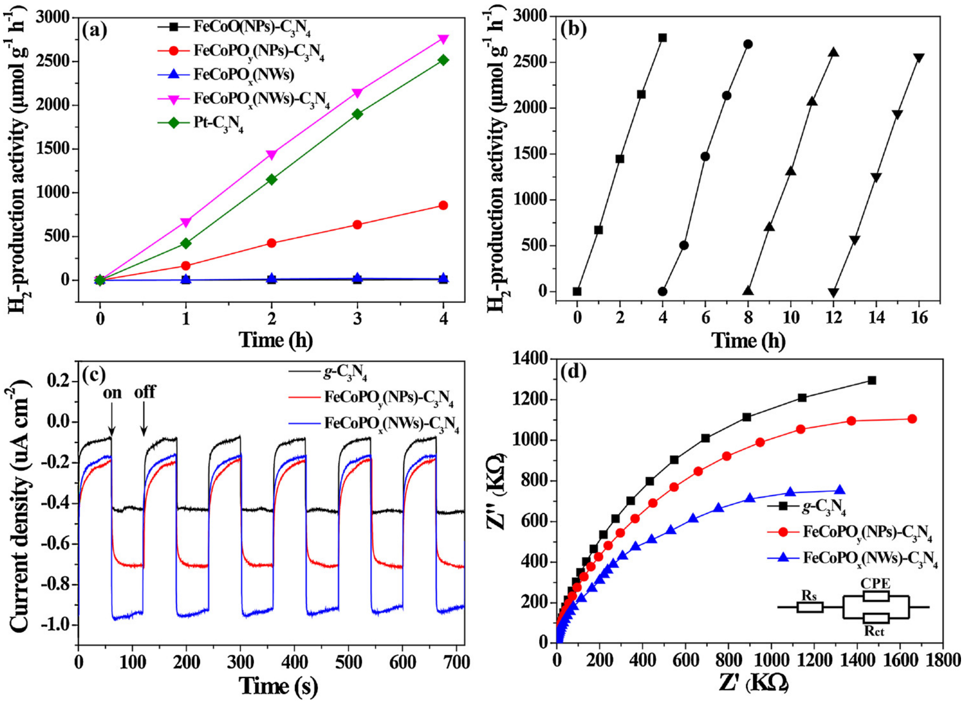

Fig. 3. The H_2-production performance. (a) Typical time course of H_2 productions under visible light (> 420 nm) irradiation on FeCoO(NPs)-C_3N_4, $FeCoPO_y$(NPs)-C_3N_4, $FeCoPO_x$(NWs), $FeCoPO_x$(NWs)-C_3N_4 and Pt-C_3N_4 photocatalysts. (b) The cycling H_2production activity of $FeCoPO_x$(NWs)-C_3N_4. (c) Photocurrent response versus time of as-prepared $FeCoPO_y$(NPs)-C_3N_4 and $FeCoPO_x$(NWs)-C_3N_4 in 0.5 M Na_2SO_4 aqueous solution under Xe lamp irradiation with the light filter of 420 nm. (d) EIS curves of as-prepared $FeCoPO_y$(NPs)-C_3N_4 and $FeCoPO_x$(NWs).

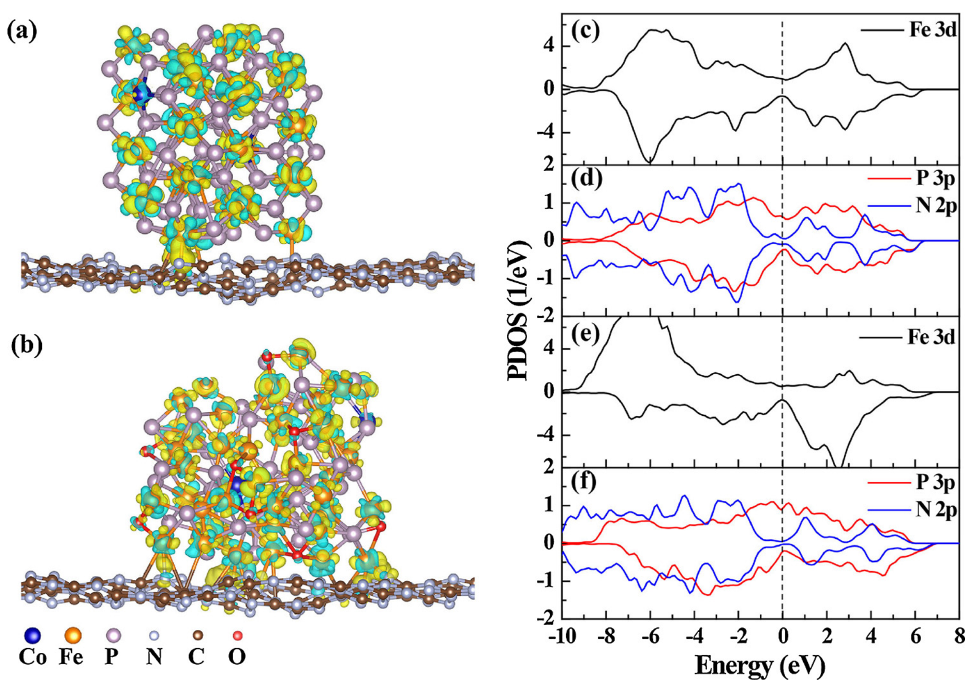

Fig. 4. The charge density difference maps of (a) $FeCoPO_y$(NPs)-C_3N_4 and (b) $FeCoPO_x$(NWs)-C_3N_4. The projected density of state (PDOS) plots of (c and d) the interfacial atoms on $FeCoPO_y$(NPs)-C_3N_4 and (e and f) $FeCoPO_x$(NWs)-C_3N_4.

the enhanced charge separation in the $FeCoPO_x$(NWs)-C_3N_4. The obtained results show that EIS Nyquist plot of $FeCoPO_x$(NWs)-C_3N_4 owns the smallest arc radius compared to that of bare g-C_3N_4 or $FeCoPO_y$(NPs)-C_3N_4. The Nyquist plot is fitted tothe equivalent Randle circuit (inset in Fig. 3d), where R_s is the electrolyte solution resistance, CPE is the constant phase element for the electrode and electrolyte interface, and R_{ct} is the interfacial charge transfer resistance across the electrode-electrolyte. Those results suggest that $FeCoPO_x$(NWs)-C_3N_4 has thefastest interfacial charge transfer and the most efficient separation of photo-generated charge carriers.

In general, the Fe-P site has a higher H_2-production activity than Fe-O site. However, the $FeCoPO_x$(NWs)-C_3N_4 with less Fe-P sites shows a larger H_2-production rate than $FeCoPO_y$(NPs)-C_3N_4 with more Fe-P sites. This implies that other factor determines the H_2-production activity of $FeCoPO_x$(NWs)-C_3N_4. Commonly, the amorphous catalystis located in a metastable state, tending to be exposed with the low-coordination atoms [27]. Those atoms have higher bonding ability or special electronic properties, which are often considered as the active reaction centers. However, for a cocatalyst in the photocatalytic reaction, the ability for capturing photogenerated charges from the photocatalyst is another key factor in influencing the performance of photocatalyst. An optimized interface between cocatalyst and photocatalyst

can provide a low barrier for charge transfer, which is preferred for a photocatalytic reaction. Considering the limitation of experimental method in studying the relationship between performance and structure at atomic level, we used the first-principles simulation to investigate the geometry structure and charge-transfer property of $FeCoPO_x$(NWs)-C_3N_4. One amorphous cluster containing 56 Fe atoms, 2 Co atoms, 47 P atoms and 9 O atoms was used to simulate the $FeCoPO_x$(NWs). For a comparison, the model of $FeCoPO_y$(NPs) with 54 Fe atoms, 2 Co atoms and 56 P atoms was also built from the supercell cell of orthorhombic FeP. A periodic atomic layer containing 96 C atoms and 128 N atoms was used to simulate the g-C_3N_4.

After geometry optimization, the obtained models are shown in Fig. S10. It is found that the $FeCoPO_y$(NPs)/$FeCoPO_x$(NWs) in two models are loaded on g-C_3N_4 surface by forming Fe-N bond. It is not strange because the partial N atoms in g-C_3N_4 are two-fold coordinated and negatively charged, which are easier to bond with the positively charged Fe atoms compared to those three-fold coordinated C atoms. However, the difference is that more Fe-N bonds are formed between the amorphous $FeCoPO_x$(NWs) and g-C_3N_4. As a result, the corresponding charge density difference maps show that the stronger charge transfer occurs between the amorphous $FeCoPO_x$(NWs) and g-C_3N_4 (Fig. 4a and b). The large difference between the adsorption types of crystalline $FeCoPO_y$(NPs) and amorphous $FeCoPO_x$(NWs) is considered from their different structure features. For the crystalline $FeCoPO_y$(NPs), the coordination saturation of surface atoms is higher than that of amorphous $FeCoPO_x$(NWs), which is verified by the results of XAFS. As a result, the crystalline $FeCoPO_y$(NPs) shows weaker bonding interaction with g-C_3N_4. Besides, the formation of interface between two solids is also influenced by their bulk structures. In the formation process of interface, the surface atoms receive the attraction from the atoms in the bulk. As a metastable phase, the amorphous $FeCoPO_x$(NWs) easily adapts its bulk structure to the change induced by the formation of interface on the thermodynamics. Thus the amorphous $FeCoPO_x$(NWs) in the structure optimization can overcomethe constraint from the bulk atoms and form more Fe-N bonds with g-C_3N_4 to decrease the free energy of system. Thus more electron transfer channels can be formed between $FeCoPO_x$(NWs) and g-C_3N_4.

The electronic properties of $FeCoPO_y$(NPs)-C_3N_4 and $FeCoPO_x$(NWs)-C_3N_4 are further investigated by calculating the projected density of states (PDOS). The results show that the g-C_3N_4 in the $FeCoPO_x$(NWs)-C_3N_4 owns a narrowed band gap compared to that in the $FeCoPO_y$(NPs)-C_3N_4 (Fig. S11). Besides, the Fermi level in $FeCoPO_x$(NWs) show an observed improvement, implying the electron transfer from g-C_3N_4 to $FeCoPO_x$(NWs). The more detailed investigation in the reason causing above change is conducted by calculating the PDOS of interfacial atoms. The results reveal that the Fe 3d and P 3p states in the crystalline $FeCoPO_y$(NPs) own a weaker polarization than those in the amorphous $FeCoPO_x$(NWs) (Fig. 4c–f). Especially, in the amorphous $FeCoPO_x$(NWs), the Fe $3d_{down}$ states are localized in the bottom of conduction band (Fig. 4e). This can effectively reduce the energy gap of electron transfer from the N 2p states to Fe 3d states. As a result, an enhanced charge separation easily occurs in the $FeCoPO_x$(NWs)-C_3N_4, which also contributions to its high H_2-production.

4. Conclusions

To summarize, we prepared an amorphous $FeCoPO_x$(NWs)-loaded C_3N_4 photocatalyst. The amorphous $FeCoPO_x$(NWs)-C_3N_4 owns a 3.5-fold higher H_2-production rate than the crystalline $FeCoPO_y$(NPs)-C_3N_4, which is similar to the Pt-C_3N_4. The structure analysis based on XAFS reveals that the Fe species in $FeCoPO_x$(NWs)-C_3N_4 owns a lower coordination number than that in $FeCoPO_y$(NPs)-C_3N_4. The first-principles simulation shows that the metastable feature of amorphous $FeCoPO_x$(NWs) promotes the formation of more Fe-N bonds. Simultaneously, a strong interfacial electronic effect between the amorphous $FeCoPO_x$(NWs) and g-C_3N_4 is revealed, which contributes to the high H_2-production activity. This study introduces a new insight into tuning the interface between cocatalyst and photocatalyst for the enhanced charge transfer.

Acknowledgements

The authors are grateful for the financial supports of this work from the National Natural Science Foundation of China (Grant No. 51671003), the National Basic Research Program of China (Grant No. 2016YFB0100201) and start-up support from Peking University and the Young Thousand Talented Program.

Appendix A. Supplementary data

Supplementary material related to this article can be found, in the online version, at doi:https://doi.org/10.1016/j.apcatb.2018.07.007.

References

[1] Y.P. Yuan, L.W. Ruan, J. Barber, S.C.J. Loo, C. Xue, Energy Environ. Sci. 7 (2014) 3934–3951.
[2] X. Li, J.G. Yu, J.X. Low, Y.P. Fang, J. Xiao, X.B. Chen, J. Mater. Chem. A 3 (2015) 2485–2534.
[3] J.R. Ran, J. Zhang, J.G. Yu, M. Jaroniec, S.Z. Qiao, Chem. Soc. Rev. 43 (2014) 7787–7812.
[4] H.L. Wang, L.S. Zhang, Z.G. Chen, J.Q. Hu, S.J. Li, Z.H. Wang, J.S. Liu, X.C. Wang, Chem. Soc. Rev. 43 (2014) 5234–5244.
[5] L.Q. Jing, W. Zhou, G.H. Tian, H.G. Fu, Chem. Soc. Rev. 42 (2013) 9509–9549.
[6] S. Bai, J. Jiang, Q. Zhang, Y.J. Xiong, Chem. Soc. Rev. 44 (2015) 2893–2939.
[7] X. Li, J.G. Yu, M. Jaroniec, Chem. Soc. Rev. 45 (2016) 2603–2636.
[8] Y.F. Xu, C. Zhang, L.X. Zhang, X.H. Zhang, H.L. Yao, J.L. Shi, Energy Environ. Sci. 9 (2016) 2410–2417.
[9] F.F. Schweinberger, M.J. Berr, M. Doblinger, C. Wolff, K.E. Sanwald, A.S. Crampton, C.J. Ridge, F. Jackel, J. Feldmann, M. Tschurl, U. Heiz, J. Am. Chem. Soc. 135 (2013) 13262–13265.
[10] H.F. Liang, A.N. Gandi, D.H. Anjum, X.B. Wang, U. Schwingenschlogl, H.N. Alshareef, Nano Lett. 16 (2016) 7718–7725.
[11] Y.W. Tan, H. Wang, P. Liu, C. Cheng, F. Zhu, A. Hirata, M.W. Chen, Adv. Mater. 28 (2016) 2951–2955.
[12] J.H. Yang, D.G. Wang, H.X. Han, C. Li, Acc. Chem. Res. 46 (2013) 1900–1909.
[13] K.F. Wu, Z.Y. Chen, H.J. Lv, H.M. Zhu, C.L. Hill, T.Q. Lian, J. Am. Chem. Soc. 136 (2014) 7708–7716.
[14] W. Liu, L.L. Cao, W.R. Cheng, Y.J. Cao, X.K. Liu, W. Zhang, X.L. Mou, L.L. Jin, X.S. Zheng, W. Che, Q.H. Liu, T. Yao, S.Q. Wei, Angew. Chem. Int. Ed. 56 (2017) 9312–9317.
[15] J.P. Perdew, Y. Wang, Phys. Rev. B 45 (1992) 13244–13249.
[16] J.P. Perdew, K. Burke, M. Ernzerhof, Phys. Rev. Lett. 77 (1996) 3865–3868.
[17] H.J. Monkhorst, J.D. Pack, Phys. Rev. B 13 (1976) 5188–5192.
[18] J. Masa, P. Weide, D. Peeters, I. Sinev, W. Xia, Z.Y. Sun, C. Somsen, M. Muhler, W. Schuhmann, Adv. Energy Mater. 6 (2016).
[19] J.W. Hall, N. Membreno, J. Wu, H. Celio, R.A. Jones, K.J. Stevenson, J. Am. Chem. Soc. 134 (2012) 5532–5535.
[20] Y.J. Li, H.C. Zhang, M. Jiang, Y. Kuang, X.M. Sun, X. Duan, Nano Res. 9 (2016) 2251–2259.
[21] H.J. Yu, R. Shi, Y.X. Zhao, T. Bian, Y.F. Zhao, C. Zhou, G.I.N. Waterhouse, L.Z. Wu, C.H. Tung, T.R. Zhang, Adv. Mater. 29 (2017).
[22] G.G. Zhang, G.S. Li, Z.A. Lan, L.H. Lin, A. Savateev, T. Heil, S. Zafeiratos, X.C. Wang, M. Antonietti, Angew. Chem. Int. Ed. 56 (2017) 13445–13449.
[23] Y.W. Tan, H. Wang, P. Liu, Y.H. Shen, C. Cheng, A. Hirata, T. Fujita, Z. Tang, M.W. Chen, Energy Environ. Sci. 9 (2016) 2257–2261.
[24] M.A. Li, T.T. Liu, X.J. Bo, M. Zhou, L.P. Guo, S.J. Guo, Nano Energy 33 (2017) 221–228.
[25] P. Niu, L.L. Zhang, G. Liu, H.M. Cheng, Adv. Funct. Mater. 22 (2012) 4763–4770.
[26] F. Luo, H.L. Su, W. Song, Z.M. Wang, Z.G. Yan, C.H. Yan, J. Mater. Chem. 14 (2004) 111–115.
[27] J. Staszak-Jirkovsky, C.D. Malliakas, P.P. Lopes, N. Danilovic, S.S. Kota, K.C. Chang, B. Genorio, D. Strmcnik, V.R. Stamenkovic, M.G. Kanatzidis, N.M. Markovic, Nat. Mater. 15 (2016) 197–203.